Microstructure and Properties of Aluminum Alloy/ Stainless Steel Gas Tungsten Arc Fusion-Brazed Joints

A novel weld design was developed to improve the apparent tensile properties of AA5052 aluminum alloy/304 stainless steel fusion-brazed joints

BY Y. MA, P. LI, D. ZHOU, AND H. DONG

Abstract

Replacing steel with aluminum alloy is appealing for achieving structural lightweighting, so it is inevitable that these materials would be welded in products. A novel weld design was developed to improve the apparent tensile properties of AA5052 aluminum alloy/304 stainless steel fusion-brazed joints. The apparent measured strength of the flared groove joints reached 182 MPa. When the number of cyclic loadings was 10^6 times, the fatigue maximum stress of the butt joints with this joint design reached 65.3 MPa. The fatigue data were analyzed statically using Weibull distribution, then the fatigue life prediction model of the butt joints with the novel joint design was established under different stress levels.

Keywords

- Aluminum Alloy/Stainless Steel Dissimilar Joint
- Microstructure
- Tensile Property
- Fatigue Property

Introduction

The design and preparation of lightweight structural components can effectively improve the comprehensive performance of structural components, reduce energy consumption, and reduce pollutant emissions. For every 1% of weight loss of transportation vehicles, the fuel energy utilization rate improves by 8–10% (Ref. 1). Steel has the advantages of low price, high strength, good plasticity, and toughness, and it is widely used in fields such as automobile manufacturing, shipbuilding, and aerospace. However, the density of steel is relatively high (7.8 g/cm^3). Aluminum alloys have low density (2.7 g/cm^3), high strength and plasticity, and corrosion resistance. Aluminum/steel composite structures could reduce the overall weight of structural components while ensuring their strength, meeting the needs of lightweight structure development.

Aluminum/steel composite structures are used in automotive, marine, and aerospace manufacturing (Refs. 2–4). When using traditional fusion welding methods to weld aluminum and steel, hard and brittle intermetallic compounds (IMCs) are easily generated in the joint, decreasing its mechanical properties. By using solid-state welding techniques such as diffusion welding, explosive welding, and friction welding, the generation of IMCs can be reduced by controlling welding heat input. However, these methods are limited by the size of the workpiece and the type of the joint. The use of a fusion brazing process can avoid the above problems. On the one hand, there are various types of fusion-brazed joints, including butt and lap joints, and the size of the workpiece is not affected (Refs. 5–7). On the other hand, the fraction of IMCs can be controlled by the heat input of fusion-brazing. Gas tungsten arc welding (GTAW) is strong, adaptable to the environment, and easy to operate. If GTAW can be used as a heat source to achieve high-quality welds of aluminum/steel dissimilar metals, it will further promote the application of aluminum/steel composite structures.

Dong et al. (Refs. 8, 9) achieved GTAW fusion brazing of aluminum alloy and steel with ZnAl15 flux cored welding wire (with $CsAlF_4$ as the flux core component). After postweld heat treatment, the coarse Zn-rich particles at the weld seam/steel interface dissolved, and joint strength increased to 180 MPa.

https://doi.org/10.29391/2025.104.018

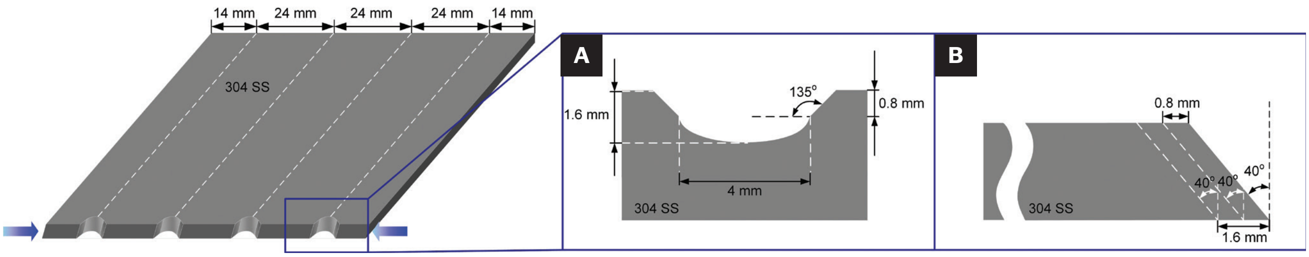

Fig. 1 — Position and dimension of flared groove design on the stainless steel side of butt joints: A — Top view; B — side view.

Table 1 — Chemical Composition of the Experimental 304SS and AA5052 (wt-%)

Materials	C	Cr	Ni	Mn	Si	Mo	Cu	Al	Mg	Zn	Fe
304SS	≤ 0.01	19.13	8.21	1.09	0.39	0.017	–	–		–	Bal.
AA5052	–	0.18	–	< 0.01	0.04	–	< 0.01	Bal.	2.63	0.01	0.16

Table 2 — Chemical Composition of the Experimental ZnAl22 Filler Wire (wt-%) (Ref. 14)

Filler Wire	Ni	Fe	Cu	Ag	Al	Zn
ZnAl22	0.003	0.033	0.002	0.001	22	Bal.

The fracture position was transferred from the IMCs layer on the steel side to the heat-affected zone on the aluminum alloy side. Lin et al. (Ref. 10) and Song et al. (Ref. 11) developed a NOCOLOK flux (65 wt-% $KAlF_4$ and 35 wt-% K_3AlF_6) + Zn + Sn pre-coating, which improved the wettability of Al-based filler wires on the surface of the steel during the aluminum/steel GTAW fusion-brazing process. The tensile strength of the joint could reach 130 MPa, and the fracture location was still at the weld seam/steel interface.

With the desire for industrial lightweighting, applying aluminum alloy/steel dissimilar metal welded joints in complex working conditions has become widespread. The fatigue properties of aluminum/stainless steel welded joints must be measured to improve the safety, reliability and service life of welded structures. Uzun et al. (Ref. 12) found that when the number of cycles for aluminum alloy/steel friction-stir-welded butt joints reached 10^7, the fatigue stress amplitude of the joint was about 60 MPa. According to the fracture morphology and path, the crack originated in the aluminum alloy at the weld toe, and the joint finally failed at the interface on the steel side. Similarly, Sandnes et al. (Ref. 13) investigated the fatigue properties of aluminum alloy/steel friction-stir-welded butt joints. The results showed that when the number of cycles was 10^6, the nominal fatigue stress range of the joint was about 90 MPa, and the failure location of the joint was mainly at the weld toe on the aluminum alloy. However, the fatigue properties of aluminum/steel welded joints need further investigation.

In this paper, a new groove design for GTAW fusion brazing to improve the apparent strength of the weld seam/stainless steel interface was examined. The microstructure of the joint was investigated. The mechanism of joint tensile property improvement was studied. The fatigue performance of the joint was analyzed statistically. A fatigue life prediction model of the joint was established.

Experimental Procedure

The base material was 5052 aluminum alloy (AA5052) and 304 stainless steel (304SS) with dimensions of 100 mm × 80 mm × 3 mm. The microstructure of the 304SS at room temperature was austenite. The chemical composition of the base metal is shown in Table 1. The flux-cored filler wire ZnAl22 was selected to weld aluminum alloy and stainless steel. The main component of the flux-core was non-corrosive NOCOLUK flux (65 wt-% $KAlF_4$ and 35 wt-% K_3AlF_6).

To increase the metallurgical bonding area and change the stress state of the aluminum alloy/stainless steel fusion-brazed joint, a flared joint design was designed at the edge of the stainless steel plate, as shown in Fig. 1. Different from the groove design of references 8 and 9, this structure transformed the weld seam/stainless steel flat interface into a curved interface that was also beveled. An aluminum alloy/stainless steel GTAW fusion-brazed joint was developed in the form of a butt joint. The schematic diagram of the welding process is shown in Fig. 2. It should be noted that the joint prep angle of the 5052 Al differed from that for 304SS. Because the weak area of the joint is the weld seam/stainless steel interface, the curved interface was only introduced on the steel side and not on the aluminum alloy side. The torch

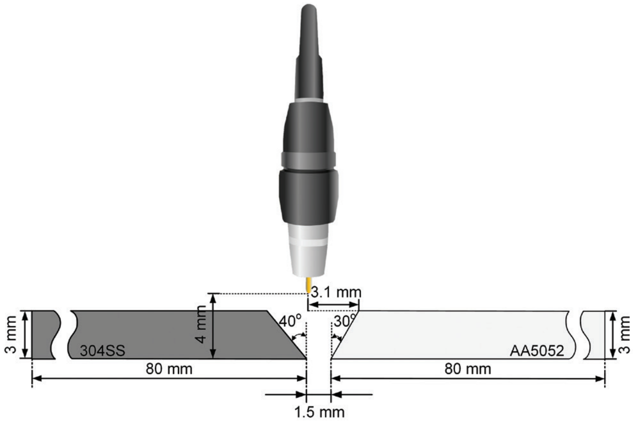

Fig. 2 — Schematic diagram of assembly before GTAW fusion-brazing.

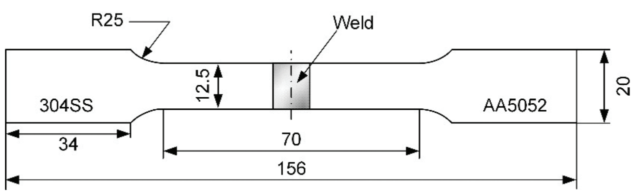

Fig. 3 — Dimension of tensile specimens for butt joints (unit: mm).

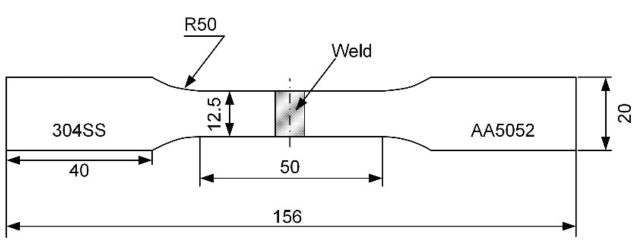

Fig. 4 — Dimensions of fatigue specimens for butt joints (unit: mm).

position was closer to the 304SS side. Jacome et al. (Ref. 15) improved the aluminum alloy/steel welded joint strength by increasing the metallurgical bonding area of the weld seam/steel interface.

The welding process was conducted by a YC-500WX4N GTAW machine with an automatic traveling device and wire feeder. The electrode diameter was 2.4 mm, and the tip was about 10–15 deg. The welding parameters for the flared groove joint were selected: the welding speed was 2 mm/s, the welding current was 110 A, and the wire feed speed was 24 mm/s. To ensure that the liquid filler metal was filled into the groove during the welding process, avoid non-fusion and slag inclusion defects, and reduce the stress concentration caused by the sharp structure, the groove was designed to have a flared shape with a 135 deg angle, as shown in Fig. 1A.

After welding, each weld had three test pieces cut out by using electrical discharge machining. The microstructure of the weld/seam interface, weld seam, and weld seam/aluminum alloy fusion zone were examined with electron probe microanalysis (EPMA, JXA-8350 F Plus). To reveal the local residual strain of the weld seam, electron backscatter diffraction (EBSD) analysis was performed by a scanning electron microscope in the KAM (kernel average misorientation) mode equipped with a field emission gun, operating at an acceleration voltage of 20 kV and a working distance of 16 mm. A Bruker Hysitron TI 980 nanoindentation instrument was used to test the hardness of the weld seam/stainless steel interface layer. The indenter was a standard Berkovich indenter, the distance between two adjacent test points was 2 µm, and the test load was 2 mN. A DSN-100 universal testing machine was employed to measure the apparent strength of AA5052/304SS joints with a displacement rate of 0.5 mm/min. The dimension of the tensile specimen is shown in Fig. 3. After the tensile test was completed, the fracture morphology was observed by scanning electron microscopy (SEM, Zeiss SUPRA 55).

A Landmark 370.250 electro-hydraulic servo fatigue testing machine manufactured by MTS was used to test the fatigue property of aluminum alloy/stainless steel fusion-brazed joints. The fatigue tests were carried out at room temperature in constant amplitude stress sine wave loading mode. The vibration frequency was 20 Hz, the load ratio was $R = F_{min}/F_{max} = 0.1$, and the maximum cyclic stress loads were 102.7 MPa, 80.3 MPa, 74.7 MPa, and 65.3 MPa, respectively. The size of the fatigue sample of the butt joints is shown in Fig. 4.

Results

Microstructure

The macro-morphology and section of the butt joint with the flared groove are shown in Fig. 5. The front and rear of the weld seam were produced continuously without macro welding defects, and the weld seam/stainless steel interface was well joined without micro-cracks.

To investigate the effect of the flared groove on the microstructure of the weld seam/stainless steel interface of the butt joint, EPMA backscattering electron imaging was performed on the longitudinal section of the joint. According to the Fe-Al-Zn phase diagram (Ref. 16), the weld seam/stainless steel interface appeared consistent with the existence of gray η-$Fe_2Al_5Zn_{0.4}$(layer I) and white η-Zn(Al)(layer II). Tan et al. (Ref. 14) also found $Fe_2Al_5Zn_{0.4}$ at the weld seam/steel interface. Yang et al. (Ref. 17) indicated that $Fe_2Al_{5-x}Zn_x$ was a non-stoichiometric variation of Fe_2Al_5. Therefore, it shares the same crystallographic structure with Fe_2Al_5 and has lattice constants similar to Fe_2Al_5, viz., orthorhombic (lattice constants: a = 0.7656 nm, b = 0.6415 nm, c = 0.4218 nm). Elemental mapping scanning analysis was conducted on the weld seam/stainless steel interface at the bottom of the flared groove (blue rectangular box in Fig. 6E), as depicted in Fig. 7. The main elements Fe, Cr, and Ni in 304SS dissolved into the weld seam, and there was a Zn-rich particle phase in η-$Fe_2Al_5Zn_{0.4}$. From our previous studies (Ref. 18), the type of intermetallic compounds generated at the weld seam/

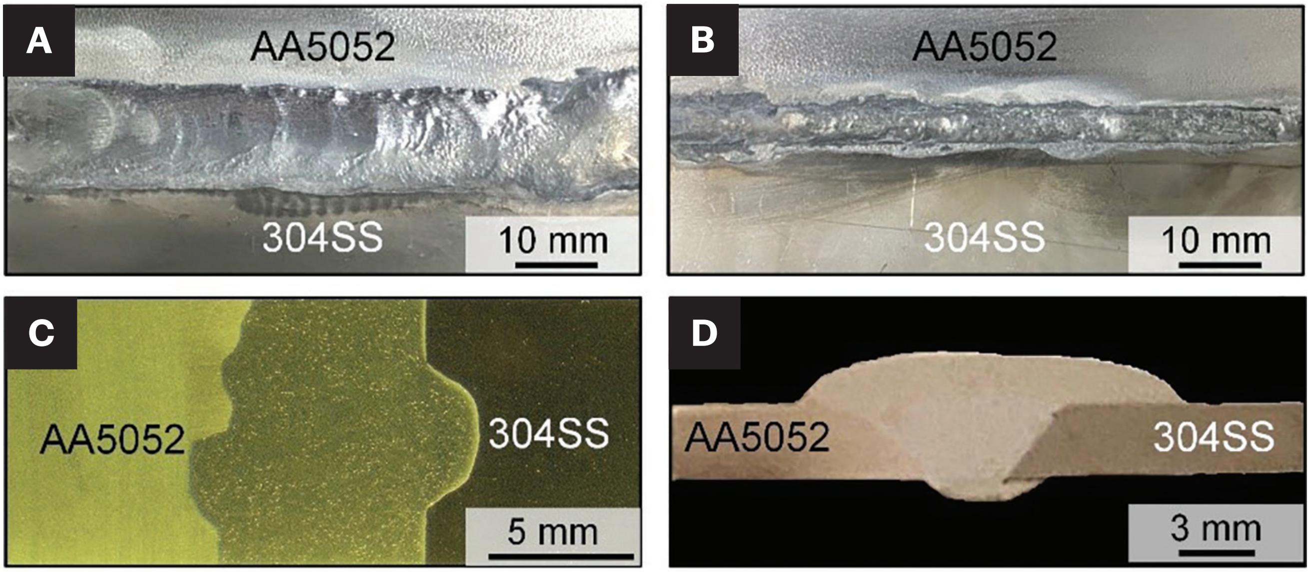

Fig. 5 — Weld appearance and sections of flared groove joints with: A — Front surface; B — rear surface; C — longitudinal section near the middle of thickness; D — cross section.

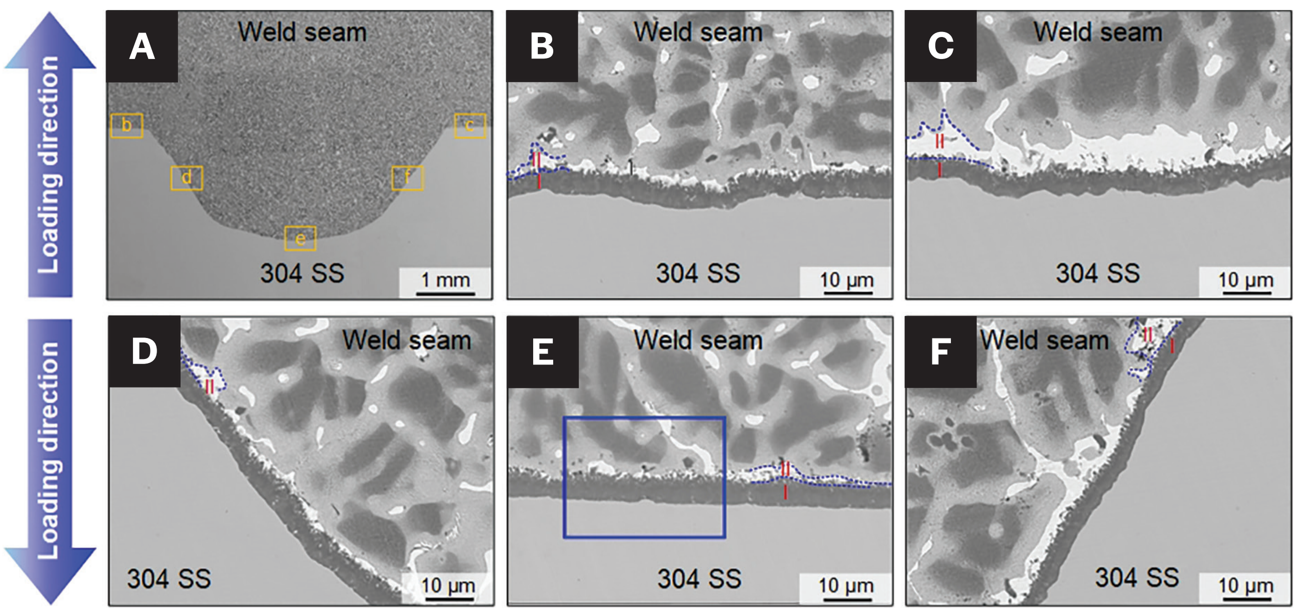

Fig. 6 — Microstructural map of stainless steel side of joint with five magnified regions. Note that the blue rectangular area is shown with composition analysis in Fig. 7.

stainless steel interface of the traditional joints were the same as in the flared groove joint of the structure.

The weld seam was composed of white η-Zn(Al), white Zn-Al eutectic, and gray α-Al, as shown in Fig. 8A. The gray area in the weld seam was locally enlarged, and the white η-Zn(Al) distributed in α-Al, as shown in Fig. 8B. The junction of the weld seam/aluminum alloy fusion zone was layered α-Al, as shown in Fig. 8C.

The kernel average misorientation of welds on the stainless steel side in butt joints with or without flared grooves was compared and analyzed by EBSD in Fig. 9. KAM distribution qualitatively reflects the degree of uniformity of plastic deformation and can be used to estimate the stress distribution state of a weld structure. The KAM value of each data point was the average mismatch angle between central data points and other data points in a certain radius. The larger the angle, the higher the degree of plastic deformation and the corresponding dislocation density (Refs. 19, 20). The results suggested that under the same welding process parameters, the residual strain of the weld seam on the stainless steel side without the flared groove was higher.

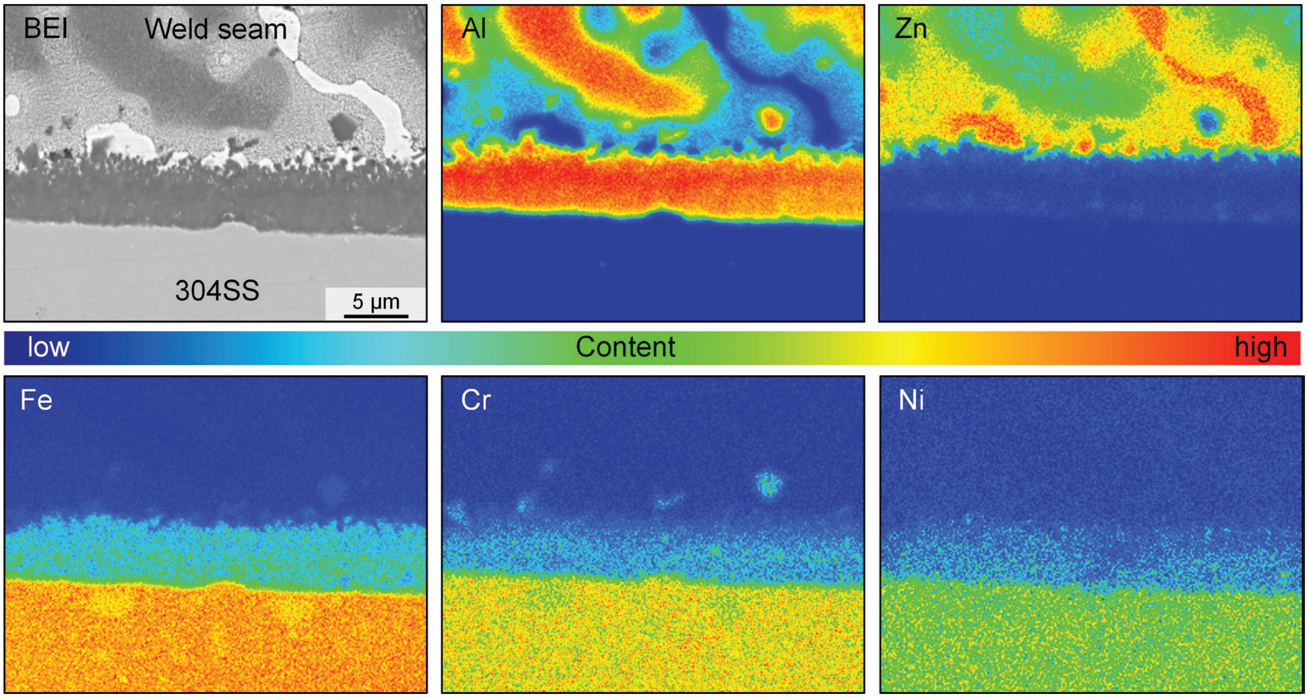

Fig. 7 — Element mapping scanning of blue rectangular area corresponding Fig. 6.

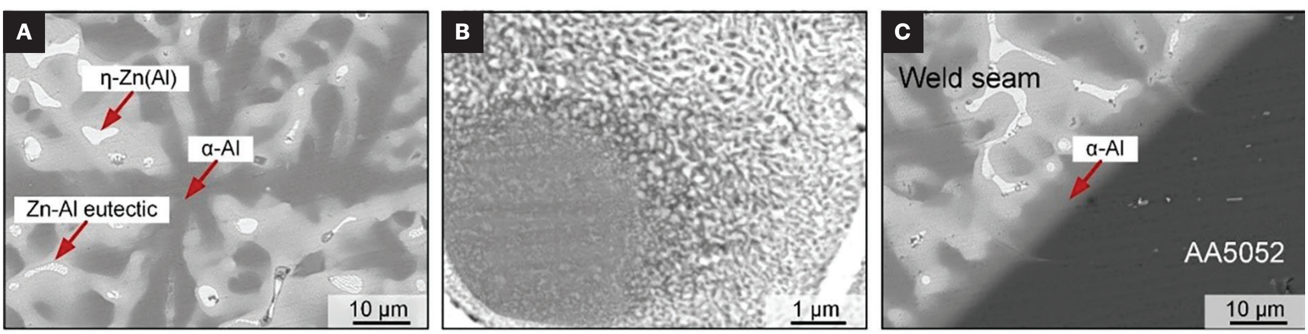

Fig. 8 — Microstructure of weld seam and weld seam/AA5052 aluminum alloy fusion zone: A — Weld seam; B — local enlarged diagram of weld seam; C — weld seam/aluminum alloy fusion zone.

Mechanical Properties

The distribution of hardness at the weld seam/stainless steel interface of the flared groove joint was measured by the nanoindentation test, as shown in Fig. 10. The results showed that the average nanoindentation hardness of interfacial layer I (the possible components were η-$Fe_2Al_5Zn_{0.4}$ and δ-$FeZn_{10}$) was 11.34 GPa, and no micro-cracks appeared near the nanoindentation.

Tensile tests were carried out on the butt joint with or without the flared groove, and the typical force-displacement curves and apparent strength of the joint are shown in Fig. 11.

After the joint reinforcement was removed, the tensile property of the flared groove joint was better than that of the joint without the flared groove under the same welding parameters. Meanwhile, the apparent strength of the flared groove joint without reinforcement was 57 MPa, 30 MPa higher than that of the normal joint without reinforcement (apparent strength 27 MPa). When the reinforcement of the joint was retained, the apparent strength of the flared groove joint reached 182 MPa.

The fracture mainly occurred at the weld seam/stainless steel interface, as shown in Figs. 12A–C. The microfracture path of the weld seam/stainless steel interface was observed by EPMA backscattering. The results showed that the cracks mainly passed through the η-$Fe_2Al_5Zn_{0.4}$/stainless steel interface, and some cracks passed through η-$Fe_2Al_5Zn_{0.4}$, as shown in Fig. 12D.

To explore the fracture characteristics of the flared groove joint in different regions, SEM observations were made on the fracture morphology, as shown in Fig. 13. The macrofracture on the stainless steel side of the joint showed that there was a strip of weld metal inside the flared groove, as shown in the blue mark in Fig. 13A. It was found that position b was flat, which indicated little ductility, as shown in Figs. 13B and b_0. The results of the EDS point analysis are listed in Table 3, and

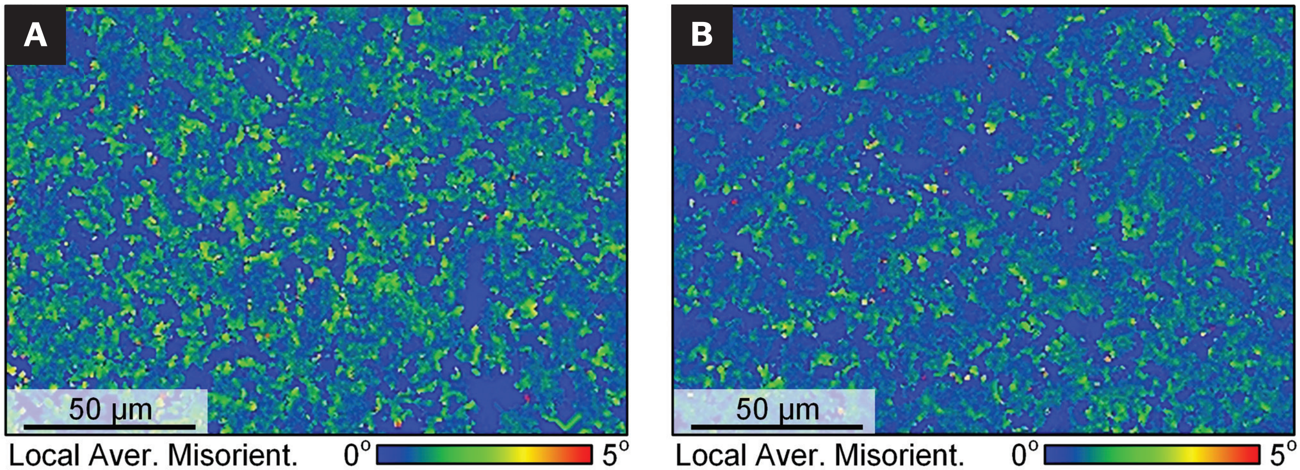

Fig. 9 — The distribution of KAM for the weld seam closed to the steel of butt joints: A — Without flared groove; B — with flared groove.

the layered structure was consistent with the stoichiometry of η-$Fe_2Al_5Zn_{0.4}$ (points A and B). Granular phases with a composition similar to η-Zn(Al) (point C) were distributed on the layered structure. Analysis indicated that when the crack propagated at the weld seam/stainless steel interface inside the flared groove, the crack was deflected toward the weld seam. A mixture of α-Al (point D) and η-Zn(Al) + α – Al (point E) was distributed on the surface of the fracture, which reflected the characteristics of mixed ductile and brittle fracture at the weld reinforcement in Figs. 13C and c_0. Compared with the fracture surface inside the flared groove (Fig. 13B), the surface roughness of the fracture in the region without the flared groove was lower. The amount of granular η-Zn(Al) (point F) decreased, and the area of layered η-$Fe_2Al_5Zn_{0.4}$ (points G, H, and I) also decreased, as shown in Figs. 13D and E. These results indicated that the cracks mainly spread at the weld seam/stainless steel interface, and the deflection behavior of the crack toward the weld seam reduced in the region without the flared groove joint.

Based on the tensile test results, after the flared groove was introduced, the butt joint showed improved tensile properties. Fatigue testing was carried out to further investigate the mechanical properties of the flared groove joint under dynamic loading. Four stress levels were selected for fatigue testing, and the maximum fatigue stresses were 102.7 MPa, 80.3 MPa, 74.7 MPa, and 65.3 MPa, respectively. The maximum fatigue stress-fatigue life curve of the flared groove joint design is shown in Fig. 14. With the decrease of the maximum stress, the number of cycles to failure increased.

The fatigue data of the flared groove joint was analyzed statistically, assuming a Weibull distribution (Ref. 21). The probability density function *f(t)* and cumulative distribution function *F(t)* were expressed as follows:

$$f(t) = \frac{\beta(t-\delta)^{\beta-1}}{\eta^{\beta}} \cdot exp^{-\left(\frac{t-\delta}{\eta}\right)^{\beta}}, t \geq \delta \qquad (1)$$

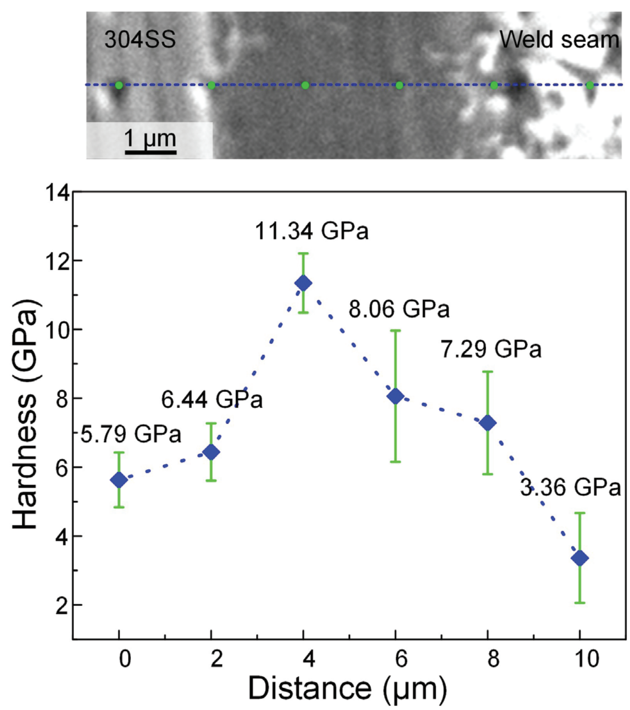

Fig. 10 — Nanoindentation hardness distribution of weld seam/stainless steel interface in the flared groove joint.

$$F(t) = \int_0^t f(t)dt = 1 - exp^{-(\frac{t-\delta}{\eta})^{\beta}} \qquad (2)$$

where β is the shape parameter, η is the size parameter, δ is the position parameter, and t is the number of cycles (Ref. 21). Fatigue tests were performed immediately after welding, so δ = 0. In the above two types, the Weibull distribution models of *f(t)* and *F(t)* were simplified as:

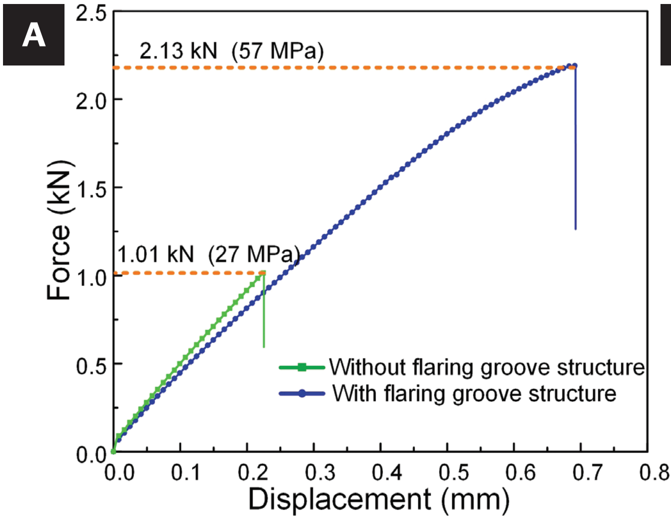

Fig. 11 — Tensile properties of butt joints with flared groove: A — Force-displacement curve of joint without weld reinforcement; B — force-displacement curve of joint with weld reinforcement.

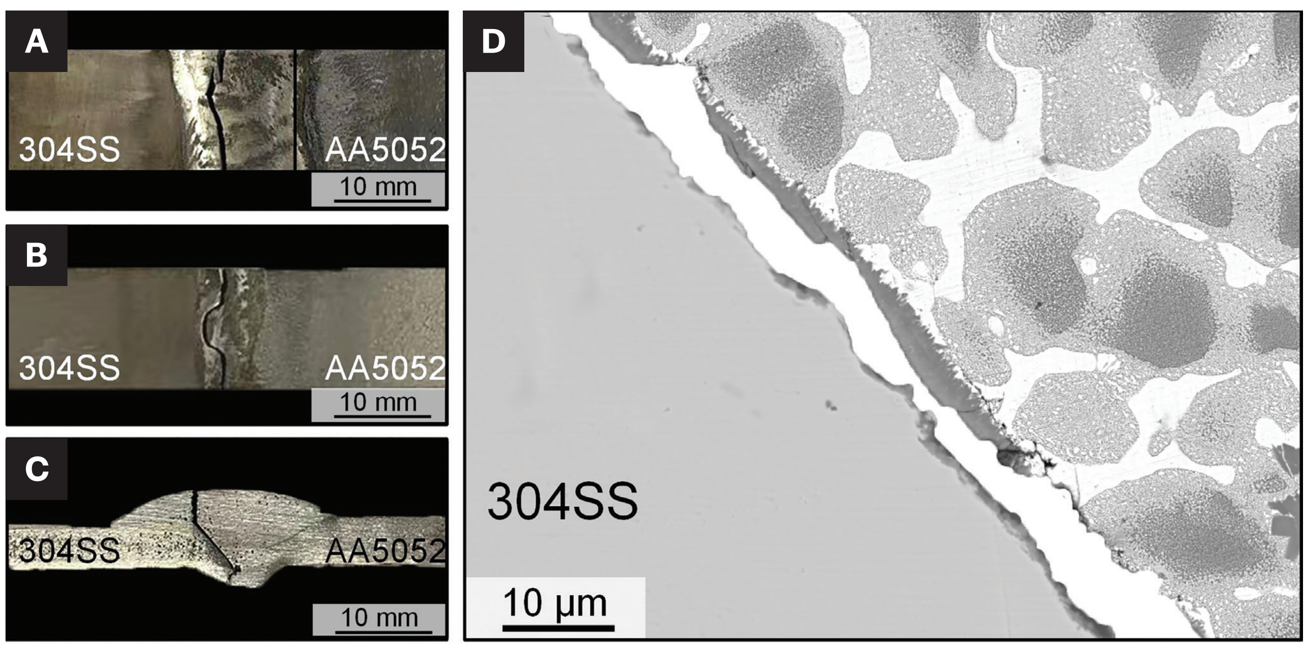

Fig. 12 — Fracture paths of the flared groove joint: A — Front surface of tensile sample; B — rear surface of tensile sample; C — cross-section of tensile sample; D — the weld seam/stainless steel interface.

$$f(t) = \frac{\beta}{\eta} \cdot (\frac{t}{\eta})^{\beta-1} \cdot exp^{-(\frac{t}{\eta})^{\beta}}, t \geq 0 \quad (3)$$

$$F(t) = 1 - exp^{-(\frac{t}{\eta})^{\beta}} \quad (4)$$

To find the values of β and η in the formula, Formula 4 can be converted to:

$$\ln\left[ln\frac{1}{R(t)}\right] = \beta\ln(t) - \beta ln\eta \quad (5)$$

When *R(t)* is defined as the reliability function, the expression is as follows:

$$R(t) = exp^{-(\frac{t}{\eta})^{\beta}} \quad (6)$$

The value of β and η can be obtained through calculating the slope and intercept of function *lnln*1/*R(t)*−ln(*t*). The value of *R* can be obtained by Bernard's median rank empirical estimation method; its expression is as follows:

$$R_i = 1 - \frac{i - 0.3}{n + 0.4} \quad (7)$$

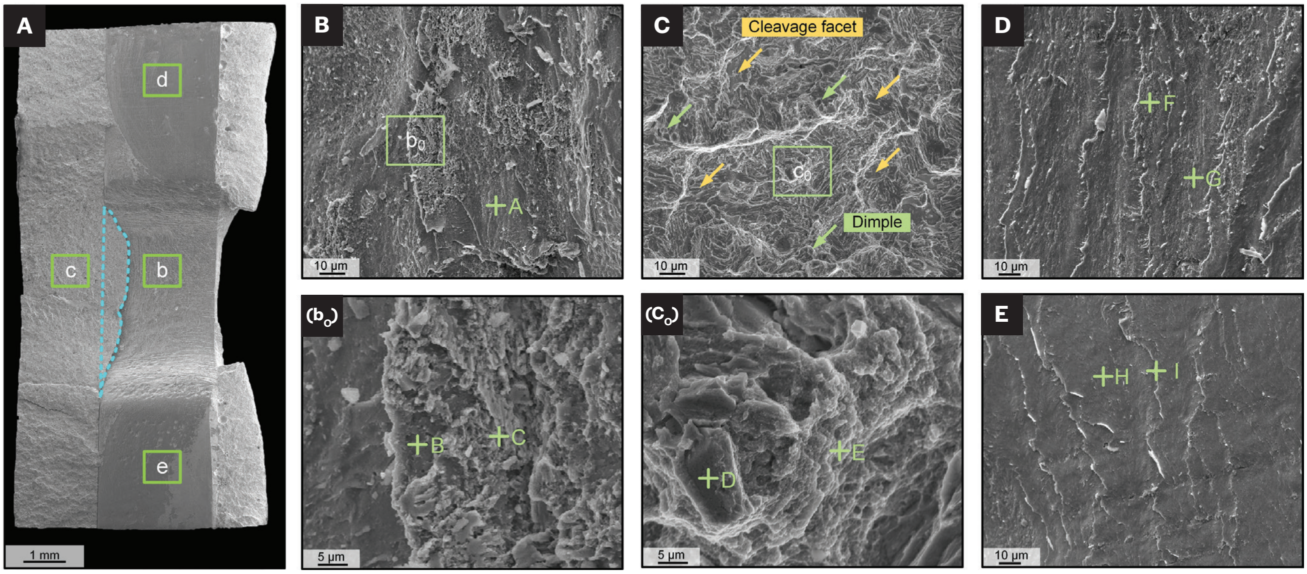

Fig. 13 — Fracture morphology of the flared groove joint with a stainless steel side: A — Macroscopic fracture morphology; B–E — locally enlarged diagram of the corresponding position in A, (b_0), and (c_0) locally enlarged diagram of the corresponding position in B and C.

Table 3 — EDS Points Analysis at the Fracture Surface in Flared Groove Joint with (at-%)

Positions	Al	Fe	Zn	Cr	Ni	Possible Phases
A	67.53	20.36	4.57	5.11	2.43	η-$Fe_2Al_5Zn_{0.4}$
B	73.64	18.83	2.33	4.21	0.99	η-$Fe_2Al_5Zn_{0.4}$
C	9.59	5.94	82.61	0.10	1.76	η-Zn(Al)
D	69.16	–	30.84	–	–	α-Al
E	37.34	–	62.66	–	–	α-Al+η-Zn(Al)
F	69.58	14.94	11.72	3.00	0.76	η-Zn(Al)+η-$Fe_2Al_5Zn_{0.4}$
G	54.57	29.12	4.62	8.82	2.87	α-Fe+η-$Fe_2Al_5Zn_{0.4}$
H	71.97	19.45	2.67	4.18	1.73	η-$Fe_2Al_5Zn_{0.4}$
I	71.36	19.24	3.59	4.39	1.42	η-$Fe_2Al_5Zn_{0.4}$

where i is the number of failed samples arranged according to the number of cycles under a given stress level, and n is the total number of samples under this stress level.

Weibull distribution model MTTF (mean time to failure), SD (standard deviation), and CV (coefficient of variation) were used to evaluate the fatigue performance and data volatility of the joint, and their expressions are as follows:

$$MTTF = \eta\Gamma(1 + \frac{1}{\beta}) \quad (8)$$

$$SD = \eta\sqrt{\left[\Gamma\left(1 + \frac{2}{\beta}\right) - \Gamma^2\left(1 + \frac{1}{\beta}\right)\right]} \quad (9)$$

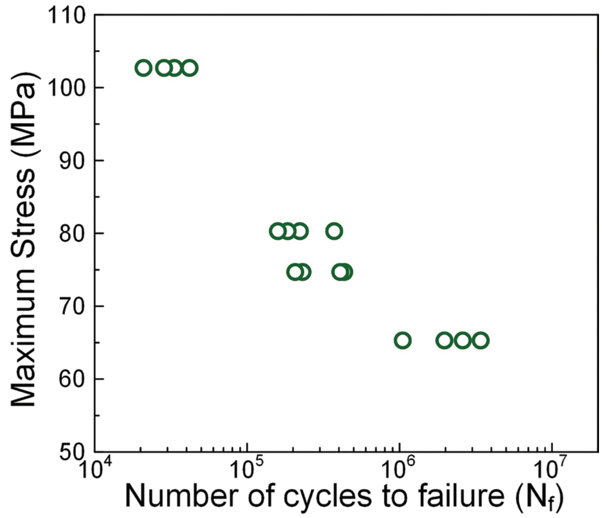

Fig. 14 — Fatigue maximum stress-fatigue life of flared groove joints.

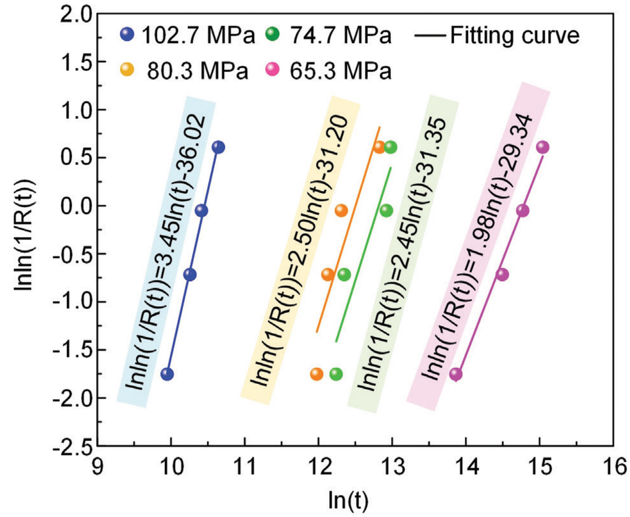

Fig. 15 — Weibull diagram of flared groove joints under different stress levels.

Table 4 — Weibull Parameters of Flared Groove Joints Under Different Stress Levels

σ_{max} (MPa)	β	η	Weibull Mean Fatigue Life, MTTF	Coefficient of Variation, CV
102.7	3.45	3.42×10^4	3.08×10^4	0.3
80.3	2.50	2.63×0^5	2.33×10^5	0.4
74.7	2.45	3.61×10^5	3.20×10^5	0.4
65.3	1.98	2.73×10^6	2.42×10^6	0.5

$$CV = \frac{SD}{MTTF} = \frac{\sqrt{\left[\Gamma\left(1+\frac{2}{\beta}\right) - \Gamma^2\left(1+\frac{1}{\beta}\right)\right]}}{\Gamma\left(1+\frac{1}{\beta}\right)} \quad (10)$$

where Γ represents the gamma function.

At a given stress level, the fatigue life of the joint can be described as:

$$N_{Rx} = \eta[-\ln(Rx)]^{-1/\beta} \quad (11)$$

where N_{RX} is the fatigue life of the joint when the reliability level is x%.

Figure 15 displays the Weibull distribution diagram of the joint under the remaining four stress levels. The values of β, η, *MTTF,* and *CV* of the flared groove joint under different stress levels calculated by linear regression method are listed in Table 4.

Through fitting the above fatigue data with the Basquin function (Ref. 22), the fatigue maximum stress-fatigue life curves of the flared groove at different reliability levels were obtained. The Basquin function expression of the fatigue maximum stress-fatigue life curve was as follows:

$$\sigma_{max} = a(N_f)^b \quad (12)$$

where σ_{max} is the maximum fatigue stress, N_f is the fatigue life, and *a* and *b* are the linear regression constants of the fatigue data.

Fatigue maximum stress-fatigue life curves of the flared groove joints at four given reliability levels (10%, 50%, and 90%) are shown in Fig. 16. In general, the higher the reliability level, the lower the corresponding fatigue maximum stress. Considering the different applications of aluminum alloy/stainless steel joints, the maximum fatigue stress-fatigue life curve under the corresponding reliability level can be selected. For example, in the aerospace field, a curve with a higher reliability level is often used to ensure the reliability and safety of the welded structure.

Discussion

The diffusion of Zn into the steel base metal can lead to grain boundary debonding and induce embrittlement of the steel base metal (Ref. 23). However, there was no evidence of Zn segregation in the steel matrix, as shown in Fig. 7, indicating that Zn did not cause embrittlement of the steel. This proved that the selection of welding process parameters was reasonable.

Wu (Ref. 24) conducted nanoindentation tests on weld seam/stainless steel interfaces of aluminum alloy/stainless steel plasma arc welding joints with AlSi filler wire. The average nanoindentation hardness values of Fe_2Al_5 were 12.0 GPa and 12.8 GPa, respectively, which were higher than the average nanoindentation hardness of Layer I at the weld seam/stainless steel interface of aluminum alloy/stainless steel joints with ZnAl22 flux-cored wire. The nanoindentation hardness of Fe-Zn phases generated in η-$Fe_2Al_5Zn_{0.4}$ was relatively low (Ref. 17). Therefore, with ZnAl22 flux-cored wire, the weld seam/stainless steel interface layer I exhibited lower hardness.

The improvement mechanism of tensile properties of the flared groove joint was analyzed. First, according to the KAM diagram of the weld seam on the stainless steel side, the residual strain of the weld metal inside the flared groove was lower than that of the joint without the flared groove. Large residual stresses and strains in aluminum alloy/stainless steel fusion-brazed joints could cause microcracks or direct cracking at the weld seam/stainless steel interface. The introduction of the flared groove in the butt joint can change the stress state of the weld seam on the stainless steel side and reduce the cracking tendency of the weld seam/stainless steel interface.

Second, for the flared groove joint, the weld seam/stainless steel interface perpendicular to the tensile direction was a curved surface; its area was larger than the flat face area without a flared groove, which effectively improved the tensile properties of the weld seam/stainless steel interface. This was confirmed by the tensile test of the butt joint after removal of reinforcements.

In summary, when the flared groove was introduced at the stainless steel base metal, the weld seam area was increased, and the types of IMCs at the weld seam/stainless steel were unchanged. Compared with traditional joints, flared groove joints have a smaller strain concentration at the weld seam adjacent to the weld seam/stainless steel interface, which resists fracture locally and provides a larger apparent strength.

Conclusions

The mechanical property and enhancement mechanism of aluminum alloy/stainless steel GTAW fusion-brazed joints with a flared groove was investigated. The main conclusions are as follows:

1. The flared groove was introduced into the butt joint to increase the metallurgical bonding area of the weld seam/stainless steel interface and modify the stress state on the interface IMCs during testing. The fracture position of the joint was located at the weld seam/stainless steel interface, and the apparent strength of the butt flared groove joints was as high as 182 MPa.

2. The fatigue life prediction model of aluminum alloy/stainless steel welded joints was established under different stress levels. When the number of cyclic loadings reached 10^6 times, the fatigue maximum stress of the flared groove joint was 65.3 MPa. The fatigue data of the flared groove joints was analyzed statistically by Weibull distribution under different reliability levels, and the σ_{max}-N_f curves were obtained.

3. The flared groove joint design can increase the apparent strength of aluminum alloy/stainless steel dissimilar welds by changing the stress state.

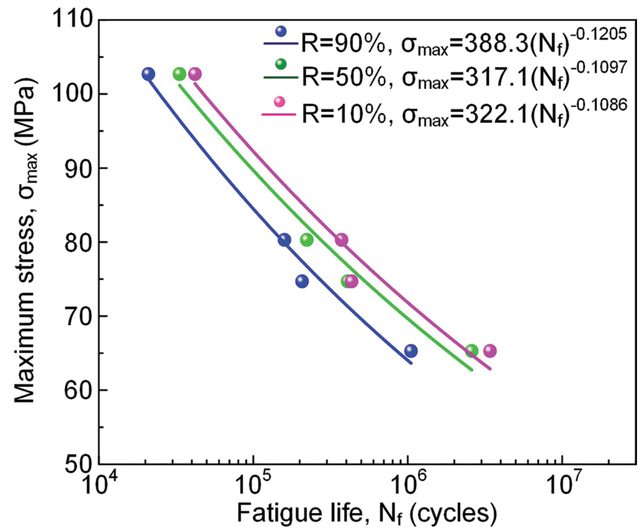

Fig. 16 — Fatigue maximum stress-fatigue life curves of flared groove joints under different reliability levels.

Acknowledgments

This work was supported by the National Natural Science Foundation of China (Grant No. 52275314), the National Key Research and Development Project (2023YFB3407500), the State Key Laboratory of Advanced Design and Manufacturing Technology for Vehicle (No. 32215003), and the Collaborative Innovation Center of Major Machine Manufacturing in Liaoning.

References

1. Danie, C. 2009. Aircraft designers shoot for savings on the wing. *Science* 325(5942): 810–811.

2. Zhang, L. P., Wen, J. P., Xie, J. P., et al. 2024. Intermetallic compounds growth and morphology evolution of Al6061/SS304 electromagnetic pulse welding joint interface during post-weld heat treatment. *Journal of Materials Research and Technology* 28: 4001–4011.

3. Becker, N., Gauthier, D., and Vidal, E. E. 2020. Fatigue properties of steel to aluminum transition joints produced by explosion welding. *International Journal of Fatigue* 139: 105736.

4. Wei, Y. N., Li, J. L, Xiong J. T., et al. 2015. Research progress in friction stir welding of aluminum/steel dissimilar metals. *Journal of Netshape Forming Engineering* 7(05): 34–39, 76.

5. Cheng, C., Meng, B., Han, J. Q., et al. 2017. A modified Lou–Huh model for characterization of ductile fracture of DP590 sheet. *Materials & Design* 118(10): 89–98.

6. Yang, L. H., Wan, Y. X., Qin, Z. L., et al. 2018. Fabrication and corrosion resistance of a graphene–tin oxide composite film on aluminium alloy 6061. *Corrosion Science* 130(9): 85–94.

7. Li, Y. J., Wang J., and Liu, Q. 2006. *Non-ferrous metal welding and application*. Beijing: Chemical Industry Press.

8. Dong, H. G., Hu, W. J., Duan, Y. P., et al. 2012. Dissimilar metal joining of aluminum alloy to galvanized steel with Al-Si, Al-Cu, Al-Si-Cu and Zn-Al filler wires. *Journal of Materials Processing Technology* 212(2): 458–464.

9. Dong, H. G., Yang, L. Q., Dong C., et al. 2012. Improving arc joining of Al to steel and Al to stainless steel. *Materials Science and Engineering: A* 534: 424–435.

10. Lin, S. B., Song, J. L., Yang, C. L., et al. 2009. Metallurgical and mechanical investigations of aluminium-steel butt joint made by tungsten inert gas welding-brazing. *Science and Technology of Welding and Joining* 14(7): 636–639.

11. Song, J. L., Lin, S. B., Yang, C. L., et al. 2009. Spreading behavior and microstructure characteristics of dissimilar metals TIG welding-brazing of aluminum alloy to stainless steel. *Materials Science and Engineering: A* 509(1–2): 31–40.

12. Uzun, H., Dalle Donne, C., Argagnotto, A., et al. 2005. Friction stir welding of dissimilar Al 6013-T4 to X5CrNi18-10 stainless steel. *Materials & Design* 26(1): 41–46.

13. Sandnes, L., Welo, T., Grong, Ø., et al. 2022. On the fatigue properties of a third generation aluminium-steel butt weld made by hybrid metal extrusion & bonding (HYB). *International Journal of Fatigue* 155: 106586.

14. Tan, C., Zang, C., Xia H., et al. 2018. Influence of Al additions in Zn–based filler metals on laser welding-brazing of Al/steel. *Journal of Manufacturing Processes* 34: 251–263.

15. Jácome, L. A., Weber, S., Leitner, A., et al. 2009. Influence of filler composition on the microstructure and mechanical properties of steel-aluminum joints produced by metal arc joining. *Advanced Engineering Materials* 11(5): 350–358.

16. Raghavan, V. 2003. Al-Fe-Zn (aluminum-iron-zinc). *Journal of Phase Equilibria* 24(6): 546–550.

17. Yang, J., Li, Y. L., Zhang, H., et al. 2015. Control of interfacial intermetallic compounds in Fe-Al joining by Zn addition. *Materials Science and Engineering: A* 645: 323–327.

18. Ma, Y. T. 2024. Microstructure and properties of AA5052 aluminum alloy/304 stainless steel tungsten inert gas arc fusion-brazed joint. Dalian University of Technology.

19. Ramazani, A., Bruehl, S., Gerber, T., et al. 2014. Quantification of bake hardening effect in DP600 and TRIP700 steels(J). *Materials and Design* 57: 479–486.

20. Zheng, G. M., Tang, B., Zhou, Q., et al. 2020. Development of a flow localization band and texture in a forged near-α titanium alloy. *Metals* 10: 121–130.

21. Haidyrah, A. S., Newkirk, J. W., and Castaño, C. H. 2016. Weibull statistical analysis of Krouse type bending fatigue of nuclear materials. *Journal of Nuclear Materials* 470: 244–250.

22. Effertz, P. S., Infante, V., Quintino, L., Suhuddin, U., Hanke, S., and dos Santos, J. F. 2016. Fatigue life assessment of friction spot welded 7050-T76 aluminium alloy using Weibull distribution. *International Journal of Fatigue* 87: 381–90.

23. Dong, W. F., Pan, H., Lei, M., et al. 2022. Zn penetration and its coupled interaction with the grain boundary during the resistance spot welding of the QP980 steel. *Scripta Materialia* 218: 114832.

24. Wu, D. 2023. Study on microstructure and mechanical properties of aluminum alloy/high strength steel dissimilar material plasma arc welding joint. Jilin University.

YUETING MA, **PENG LI**, and **HONGGANG DONG** (*donghg@dlut.edu.cn*) are with School of Materials Science and Engineering, Dalian University of Technology, Dalian, China. **DIANWU ZHOU** is with State Key Laboratory of Advanced Design and Manufacturing Technology for Vehicle Body, Hunan University, Changsha, China.